SPECIAL
Ocean Turbulence
COLLECTION

Turbulent Transition of a Flow from Small to $O(1)$ Rossby Numbers

JIM THOMAS[a,b] AND R. VISHNU[c]

[a] *International Centre for Theoretical Sciences, Tata Institute of Fundamental Research, Bangalore, India*
[b] *Centre for Applicable Mathematics, Tata Institute of Fundamental Research, Bangalore, India*
[c] *Fluid Mechanics Unit, Okinawa Institute of Science and Technology Graduate University, Okinawa, Japan*

(Manuscript received 20 November 2021, in final form 22 June 2022)

ABSTRACT: Oceanic flows are energetically dominated by low vertical modes. However, disturbances in the form of atmospheric storms, eddy interactions with various forms of boundaries, or spontaneous emission by coherent structures can generate weak high-baroclinic modes. The feedback of the low-energy high-baroclinic modes on large-scale energetically dominant low modes may be weak or strong depending on the flow Rossby number. In this paper we study this interaction using an idealized setup by constraining the flow dynamics to a high-energy barotropic mode and a single low-energy high-baroclinic mode. Our investigation points out that at low Rossby numbers the barotropic flow organizes into large-scale coherent vortices via an inverse energy flux while the baroclinic flow accumulates predominantly in anticyclonic barotropic vortices. In contrast, with increasing Rossby number, the baroclinic flow catalyzes a forward flux of barotropic energy. The barotropic coherent vortices decrease in size and number, with a strong preference for cyclonic coherent vortices at higher Rossby numbers. On partitioning the flow domain into strain-dominant and vorticity-dominant regions based on the barotropic flow, we find that at higher Rossby numbers baroclinic flow accumulates in strain-dominant regions, away from vortex cores. Additionally, a major fraction of the forward energy flux of the flow takes place in strain-dominant regions. Overall, one of the key outcomes of this study is the finding that even a low-energy high-baroclinic flow can deplete and dissipate large-scale coherent structures at $O(1)$ Rossby numbers.

KEYWORDS: Mesoscale processes; Small scale processes; Turbulence; Eddies; Anticyclones; Inertia-gravity waves

1. Introduction

A significant fraction of oceanic mesoscale flow, with lateral scales of $O(100)$ km, is in geostrophic and hydrostatic balance. These balance constraints on the flow lead to an inverse energy flux, organizing the balanced flow into large-scale coherent vortices or eddies (Scott and Wang 2005; Chelton et al. 2011). Since geostrophic energy on average gets transferred to larger scales, potential mechanisms that can break these constraints, reverse the energy flux from inverse to forward, and thereby enhance small-scale dissipation of balanced flow are actively sought after. With the mesoscale balanced flow being fed through instabilities of larger basin-scale flow, identifying potential mechanisms that can insinuate loss of balance and assist in small-scale dissipation of balanced energy is a crucial ingredient for closing the overall oceanic energy budget (Wunsch and Stammer 1998; Ferrari and Wunsch 2010).

In addition to the balanced eddies, oceanic flows are rich in inertia–gravity waves generated by atmospheric winds and gravitational tides. Contrary to the dynamics of the balanced flow, inertia–gravity waves exhibit a forward energy flux and dissipate their energy at small viscous scales. Furthermore, recent oceanic observational datasets and realistically forced global-scale ocean model outputs reveal that depending on the geographic location and season, wave energy levels can locally be comparable or stronger than balanced energy (Richman et al. 2012; Bühler et al. 2014; Qiu et al. 2017; Savage et al. 2017; Qiu et al. 2018; Tchilibou et al. 2018; Torres et al. 2018; Lien and Sanford 2019). These datasets have inspired a broad set of investigations aimed at understanding how gravity waves interact with balanced flow and modify quasigeostrophic turbulent dynamics, specifically with an eye on deducing whether waves can form an energy sink for balanced energy.

Dedicated idealized explorations using reduced asymptotic models, two-vertical-mode models, and full Boussinesq equations (Gertz and Straub 2009; Xie and Vanneste 2015; Wagner and Young 2016; Taylor and Straub 2016; Rocha et al. 2018; Thomas and Yamada 2019; Thomas and Arun 2020; Xie 2020; Thomas and Daniel 2020; Taylor and Straub 2020; Thomas and Daniel 2021) have revealed two key features of wave–balance exchanges in the small Rossby number regime. First, there is no universal energy transfer direction between waves and balanced flows: depending on the kind of wave field and relative energy levels of wave and balanced flow, waves can transfer energy to or extract energy from balanced flow (see Table 2 in Thomas and Daniel 2021). Second, waves severely modify intrinsic balanced flow dynamics, such as the inverse energy flux and formation of large-scale coherent vortices,

Corresponding author: Jim Thomas, jimthomas.edu@gmail.com

DOI: 10.1175/JPO-D-21-0270.1

only when wave energy is significantly higher than balanced energy. Specifically, waves irreversibly impact balanced flow in regimes where $E_G/E_W \lesssim \mathrm{Ro}^2$, where E_G and E_W denote balanced and waves' energies, respectively, and Ro is the Rossby number. These findings point out that the balanced flow is extremely rugged in the small Rossby number regime and can be perturbed only in the presence of high energy waves, irrespective of the kind of wave field.

A different scenario for the breakdown of balanced flow and increased small-scale dissipation of balanced energy is when the flow Rossby number departs from asymptotically small values and increases to $O(1)$ values. Such a scenario happens at oceanic submeoscales, these being flows with lateral scales ranging from 0.1 to 10 km and time scales on the order of a day. A wide range of in situ and satellite altimeter datasets along with high-resolution simulations over the past decade have identified the ubiquitous presence of energetic submesoscale flows in the world's oceans, these submesoscale flows exhibiting significant departures from balanced flow dynamics and quasigeostrophic turbulence phenomenology (Lumpkin and Elipot 2010; Shcherbina et al. 2013; Xu and Fu 2011; Capet et al. 2008; Qiu et al. 2014; Brannigan et al. 2015; Thompson et al. 2016; Buckingham 2016; Poje et al. 2017; Barkan et al. 2017; Yu et al. 2019; Erickson et al. 2020). It is noteworthy that even straightforward numerical integration of ocean models, set in boundary current regions and open ocean configurations, have found the generation of submesoscale dynamics simply by increasing the resolution of the models (Capet et al. 2008; Brannigan et al. 2015). These ocean model outputs indicate increased small-scale energy and shallower energy spectra as spatial resolution is increased, resulting in a lack of numerical convergence of the ocean model simulations with gradually increasing spatial resolution.

The widespread relevance of oceanic submesoscale flows and the limitations of ocean models in fully resolving them makes it imperative to investigate various phenomenological aspects of submesoscale flows in different configurations and understand how they depart from mesoscale dynamics characterized by asymptotically small Rossby numbers. Quasigeostrophic turbulence and our understanding of mesoscale eddy dynamics has reached a mature level, thanks to a wide range of idealized two-dimensional and three-dimensional studies that have explored intricate details of turbulent balanced flow exchanges (McWilliams 1984, 1989; Larichev and Held 1995; Smith and Vallis 2001; Nadiga 2014). Similar dedicated exploratory attempts are key to developing insights into the fluid dynamic aspects of $O(1)$ Rossby number geophysical turbulence. With these inspirations, in this paper we study a specific phenomenon: the changes accompanying the turbulent dynamics of an idealized flow across different Rossby numbers, from low Rossby number mesoscale regime to $O(1)$ Rossby number submesoscale regime.

On examining energy content in vertical modes in the ocean, theoretical estimates, idealized numerical simulations, and in situ observations reveal that most of the energy is contained in the barotropic and the first few baroclinic modes (Fu and Flierl 1980; Wunsch 1997; Smith and Vallis 2001; Zhao et al. 2018). Despite this, external perturbations such as those generated by atmospheric winds, eddies interacting with boundaries, or via spontaneous emission of high Rossby number coherent structures can lead to the excitation of high-baroclinic modes (Liang and Thurnherr 2012; Alford et al. 2013; Gula et al. 2015; Clément et al. 2016; Alford et al. 2016; Gula et al. 2016). While some specialized disturbances, such as extremely strong atmospheric storms (D'Asaro et al. 2011), can energize high-baroclinic energy levels to a degree that they are comparable or stronger than the energy content in the low modes, a wide variety of disturbances lead to configurations where the low modes still remain the dominant flow component with high-baroclinic energy levels being relatively low. Consequently, constraining the flow to the barotropic and a high-baroclinic mode gives us an idealized two-vertical-mode model that can be used to investigate the energetic interaction between a high-energy barotropic flow and a weak or low-energy high-baroclinic mode. Although the baroclinic flow remains energetically weak, the strength of the interaction may be weak or strong depending on the Rossby number of the flow.

Flows with $O(1)$ Rossby numbers are typically observed in the upper ocean in weakly sheared eddies, or as eddies interact with topographic features (Boccaletti et al. 2007; Shcherbina et al. 2013; Buckingham 2016; Callies et al. 2015; Yu et al. 2019; Thompson et al. 2016; Gula et al. 2015, 2016). These commonly observed flows serve as an inspiration for our investigation in the $O(1)$ Rossby regime, although the extreme idealization of restricting the primitive equations to two modes prevents a one-to-one correspondence between our setup and that of realistic oceanic flows. Within our idealized setup we will explore how flow structures, energy flow pathways, and various statistical quantities in physical space and spectral space change as Rossby number increases from low to $O(1)$ values.

The plan for the paper is as follows: we present the model and the parameter regimes in section 2, results in section 3, and summarize our findings in section 4.

2. The two-vertical-mode model and numerical integrations

The two-vertical-mode model used for our present study is obtained by projecting the f-plane primitive equations onto the barotropic and a single baroclinic mode imposing flat rigid lid boundary conditions on top and bottom vertical boundaries and constant buoyancy frequency. For example, the horizontal velocity field $\mathbf{v}$ is expanded in vertical modes as $\mathbf{v}(\mathbf{x},z,t) = \mathbf{v}_T(\mathbf{x},t) + \sqrt{2}\cos(n\pi z/H)\mathbf{v}_C(\mathbf{x},t)$, where $\mathbf{v}_T$ and $\mathbf{v}_C$ denote the barotropic and the baroclinic horizontal velocity fields, respectively; H is the depth of the ocean; and $\cos(n\pi z/H)$ is the nth baroclinic mode eigenfunction. Projecting the primitive equations on the barotropic and the nth baroclinic mode gives a reduced two-dimensional model. The equations so obtained were then nondimensionalized, choosing the inertial time scale $1/f$ (where f is the constant rotation rate) as the time scale and the horizontal length scale L to be the length of the domain. An arbitrary velocity scale U was used to nondimensionalize velocity fields and the geostrophic balance

condition using the velocity scale U was used to obtain the scale for baroclinic pressure (p_C). After nondimensionalizing the reduced model, we obtain the equations:

$$\frac{\partial \zeta_T}{\partial t} + \mathrm{Ro}\nabla \times [\mathbf{v}_T \cdot \nabla \mathbf{v}_T + \mathbf{v}_C \cdot \nabla \mathbf{v}_C + (\nabla \cdot \mathbf{v}_C)\mathbf{v}_C] = f_T - \nu\Delta^8 \zeta_T, \tag{1a}$$

$$\frac{\partial \mathbf{v}_C}{\partial t} + \hat{\mathbf{z}} \times \mathbf{v}_C + \mathrm{Bu}\, \nabla p_C + \mathrm{Ro}(\mathbf{v}_T \cdot \nabla \mathbf{v}_C + \mathbf{v}_C \cdot \nabla \mathbf{v}_T) = \mathbf{f}_C - \nu\Delta^8 \mathbf{v}_C, \tag{1b}$$

$$\frac{\partial p_C}{\partial t} + \nabla \cdot \mathbf{v}_C + \mathrm{Ro}(\mathbf{v}_T \cdot \nabla p_C) = -\nu\Delta^8 p_C. \tag{1c}$$

In the variables above, subscripts T and C indicate barotropic and baroclinic fields, respectively; $\mathrm{Ro} = U/fL$ represents the Rossby number; and $\mathrm{Bu} = (NH/n\pi fL)^2$ is the Burger number. The gradient operator above is $\nabla = (\partial/\partial x, \partial/\partial y)$ and the curl operator shorthand used above is $\nabla \times \mathbf{v} = \nabla \times (u, v) = \partial v/\partial x - \partial u/\partial y$. The barotropic flow is divergence free and is entirely captured by the barotropic vorticity ζ_T, which is related to the barotropic streamfunction ψ_T via $\zeta_T = \nabla \times \mathbf{v}_T = \Delta\psi_T$. The terms f_T and $\mathbf{f}_C$ in (1) denote barotropic and baroclinic forcing terms, respectively, while $\nu\Delta^8\zeta_T$, $\nu\Delta^8\mathbf{v}_C$, and $\nu\Delta^8 p_C$ are hyperdissipation terms removing energy reaching grid scale. In the absence of forcing and dissipation, (1) conserves the total flow energy

$$\int_D \left(\frac{1}{2}\mathbf{v}_T^2 + \frac{1}{2}\mathbf{v}_C^2 + \mathrm{Bu}\frac{1}{2}p_C^2\right) d\mathbf{x}, \tag{2}$$

where integration above is performed over the whole domain. The first term above is the barotropic energy while the remaining two terms form the baroclinic energy.

At this point it is worth making a digression to note that the reduced model (1) was obtained by projecting the primitive equations onto the barotropic and a high-baroclinic mode assuming rigid lid boundary conditions with vanishing vertical velocities on the top and bottom vertical boundaries. As recent work has pointed out, such a projection needs to be modified in the presence of realistic rough steep bottom topography (de La Lama et al. 2016; LaCasce 2017; LaCasce and Groeskamp 2020). In realistic oceanographic scenarios with rough bathymetry, these studies reveal that the dominant mode is the first baroclinic mode with vanishing bottom horizontal velocity. Consequently, although for the present idealized study we use the two vertical modes in (1), the model will need to significantly change to accommodate for more realistic oceanographic situations involving surface intensified flows and rough bathymetry.

Returning to our study, for the governing equations (1) we chose a high-baroclinic mode, i.e., $n \gg 1$, making the Burger number a small parameter, $\mathrm{Bu} \ll 1$. For the numerical integrations, we specifically set $\mathrm{Bu} = 0.01$. The results presented in this paper were obtained using 2/3 dealiased Fourier pseudospectral numerical integration of (1) in a doubly periodic domain with 576^2 grid points. The forcing terms in (1a) and (1b) were used to generate turbulent flows in forced-dissipative equilibrium. We chose a forcing scheme that maintains a constant energy level at low wavenumbers. For the barotropic flow, we forced the low wavenumber band $k \in (0, k_f]$ with $k_f = 5$ such that the total energy contained in the forced scales $(0, k_f]$ was enforced to be 1. For the baroclinic flow, notice that in (1b) and (1c), in the absence of the nonlinear interaction terms, we are left with the linear time evolving equations, whose solution consists of linear waves and a geostrophic balanced mode. The $k = 0$ spatially homogeneous mode is the inertial oscillation mode. We chose the baroclinic forcing such that the inertial oscillation mode was forced and maintained with energy 0.1. The forcing was therefore chosen such that the baroclinic flow is a small perturbation and 90% of the large-scale flow energy was contained in the barotropic flow. We refer the reader to the appendix for technical details of the forcing term.

The forcing scheme that maintains large-scale energy of the flow to be constant has been used in multiple turbulence studies in the past (Kaneda and Ishihara 2006; Donzis and Yeung 2010) and has notable advantages. Specifically, the forcing scheme avoids the flow to evolve in a specific way by enforcing a predetermined energy injection rate for the system. If there is an inverse flux of energy, transferring flow energy to large scales, the energy at large scales tends to increase and therefore to maintain same level of energy at large scales, forcing acts as an energy sink. On the other hand, if the flow exhibits a forward energy flux depleting energy from large scales, the forcing energizes large scales by acting as an energy source. Since the rate of energy transfer from large to small scales at different Rossby numbers is not known a priori, we used the above forcing in our study.

Our forcing scheme ensured that an energetically dominant barotropic flow was forced and maintained at large scales, while low-energy spatially homogeneous inertial oscillations were forced as a small perturbation. The inertial oscillations would interact with the barotropic flow and generate spatial scales comparable to that of the barotropic flow; see detailed discussion of this process in Thomas et al. (2017). For a comparison with our setup in the present study, the model (1) was used by Thomas and Arun (2020) to examine interactions between inertial oscillations and balanced flow in the small Rossby limit. Thomas and Arun specifically focused on the case where baroclinic mode had significantly higher energy levels than the barotropic mode, a parameter regime inspired by strong atmospheric winds exciting high-energy inertial oscillations in the upper ocean. In contrast, the present study explores the opposite regime, where the high vertical mode baroclinic flow is a small perturbation to the barotropic flow—a common scenario in the ocean—and the emphasis is on understanding how the low-energy baroclinic flow will modify the dynamics of the barotropic flow as the Rossby number increases.

3. Turbulent transition from small to O(1) Rossby numbers

We used numerical solutions of (1) to study the flow dynamics across different Rossby numbers. By forcing and maintaining low wavenumber energy as explained in the previous section, we integrated (1) with different Ro values, changing Ro from 0.1 to 1 at increments of 0.01, providing us with 91 flows characterized by a specific Ro value. Each flow, with a specific Ro, was evolved for about thousand eddy turnover time scales and was checked for forced-dissipative equilibrium, by ensuring that the barotropic and baroclinic energies, flow energy spectra, and all other statistical quantities presented in this paper reached a steady state. Out of the 91 flows, 14 did not reach equilibrium and were discarded. We therefore studied the transition from low to high Rossby numbers using the remaining 77 equilibrated flows.

Although Ro is the parameter that we varied to generate different Rossby number flows and the parameter explicitly appears in (1), we may unambiguously define the effective Rossby number of each flow as $\mathrm{Ro}_{\mathrm{eff}} = \mathrm{Ro}\zeta_{\mathrm{RMS}}$, ζ_{RMS} being computed as the time-averaged root-mean-square value of the nondimensional barotropic vorticity. (It is worth noting that based on our nondimensionalization, the barotropic vorticity is nondimensionalized by U/L to obtain the nondimensional vorticity ζ.) Hereafter we will refer to each flow by its effective Rossby number, $\mathrm{Ro}_{\mathrm{eff}}$. Based on this definition, for the lowest Rossby number flow, equilibrated by setting Ro = 0.1 in (1), we obtained $\mathrm{Ro}_{\mathrm{eff}} = 0.29$ while for the highest Rossby number case where we set Ro = 1, we obtained $\mathrm{Ro}_{\mathrm{eff}} = 3.41$.

Out of the 77 cases, Fig. 1 shows snapshots of barotropic vorticity ζ_T (left column) and baroclinic speed $\sqrt{u_C^2 + v_C^2}$ (right column) for three flows with effective Rossby numbers: $\mathrm{Ro}_1 = 0.29$, $\mathrm{Ro}_2 = 1.32$, and $\mathrm{Ro}_3 = 3.41$. For the lowest Rossby number flow shown in Fig. 1a, the barotropic flow is seen to consist of large-scale cyclonic (positive) and anticyclonic (negative) coherent vortices, with like-signed vortices merging further to grow in size. On increasing Rossby number, large-scale vortices break up into smaller fragments that span the entire domain. This feature can be seen in the intermediate Rossby number flow shown in Fig. 1c. At the highest Rossby number case shown in Fig. 1e, the domain is rich with a lot of fine-scale structures, along with smaller-scale vortices. Notice that the number and size of coherent vortices decreases from top to bottom, as Rossby number is increased. The decrease in size of flow features can also be seen in the right column of Fig. 1, showing baroclinic speed. At the lowest Rossby number, the baroclinic flow has large-scale structures, which breaks down into fine-scale flow features spread throughout the domain as Rossby number is increased. The physical structures seen in Fig. 1 is complemented by energy spectra of barotropic and baroclinic flow components shown in Fig. 2. Concomitant with the generation of smaller-scale features in the flow fields, the energy spectrum of both barotropic and baroclinic modes becomes shallower with increasing Rossby number. Notably, the barotropic spectrum shown in Fig. 2a has a slope close to -3 at low Rossby numbers, which changes to a shallow slope close to $-5/3$ at the highest Rossby number.

On comparing the energy spectrum of the barotropic and baroclinic fields in the top row of Fig. 2, it can be seen that the low wavenumber part of the energy spectrum, which contains most of the energy, has relatively lesser energy content for the baroclinic flow. This trend, however, reverses at smaller scales, as seen in Fig. 2c showing the barotropic to baroclinic energy ratio across wavenumbers: notice that although at large scales the ratio is much greater than 1, the ratio drops below 1 at smaller scales. The domain-integrated energy content in the two flow fields is quantified in Fig. 2d, which shows the barotropic and baroclinic energies of all the flows as a function of effective Rossby number. Since most of the energy is contained in large scales and since barotropic energy dominates over baroclinic energy at large scales, domain-integrated energy of the barotropic flow is about 8–10 times higher than that of the baroclinic flow. This feature can also be qualitatively inferred from the physical structure plots shown in Fig. 1—notice the color bars of the figures on the left and right—the baroclinic flow structures are weaker than the barotropic flow structures.

Recall that the forcing scheme we used ensured that the barotropic energy was maintained at 1 at large scales and baroclinic energy was 0.1 in the inertial oscillation mode. The forced inertial oscillation mode interacts with the barotropic flow and generates $k > 0$ wavenumbers in the baroclinic flow. Therefore, although large-scale barotropic energy was forced and maintained to be much higher (90% of total energy) than the baroclinic energy, as the flows develop fine-scale features and transfer energy to smaller scales, this ratio could change. Nevertheless, Fig. 2d shows that the baroclinic energy is consistently an order of magnitude lower than barotropic energy, implying that the barotropic flow remains the dominant flow component across Rossby numbers. Despite being energetically weak compared to the barotropic flow, the low-energy baroclinic flow is responsible for the significant changes in barotropic flow seen in the left column of Fig. 1.

To get a handle on the constituents of the energetically weak baroclinic flow, we decomposed it into inertia–gravity waves and geostrophically balanced mode using the linear wave-balance decomposition used in Thomas and Yamada [2019, their Eq. (2.12)] and Thomas and Arun [2020, their Eqs. (8) and (9)]. Figure 3 shows the frequency spectrum of wave (blue) and balanced (red) components. For the lowest Rossby number case shown in Fig. 3a, a clear separation can be seen between waves and balanced components. Notice how the balanced red spectrum dominates at low frequencies while the blue wave spectrum overtakes the balanced spectrum, around the inertial peak marked by a dashed vertical line and remains the dominant component at higher frequencies. In contrast, at the highest Rossby number case shown in Fig. 3b, no distinct separation is seen between wave and balanced modes. Additionally, in the high Rossby number case, the frequency spectrum of the balanced component is shallower and does not decay as rapidly as in the low Rossby number case shown in Fig. 3a. On further examining the frequencies of specific wavenumbers of the wave field (figures omitted), the wave component in the low Rossby regime was seen to have energy concentrated along frequencies dictated

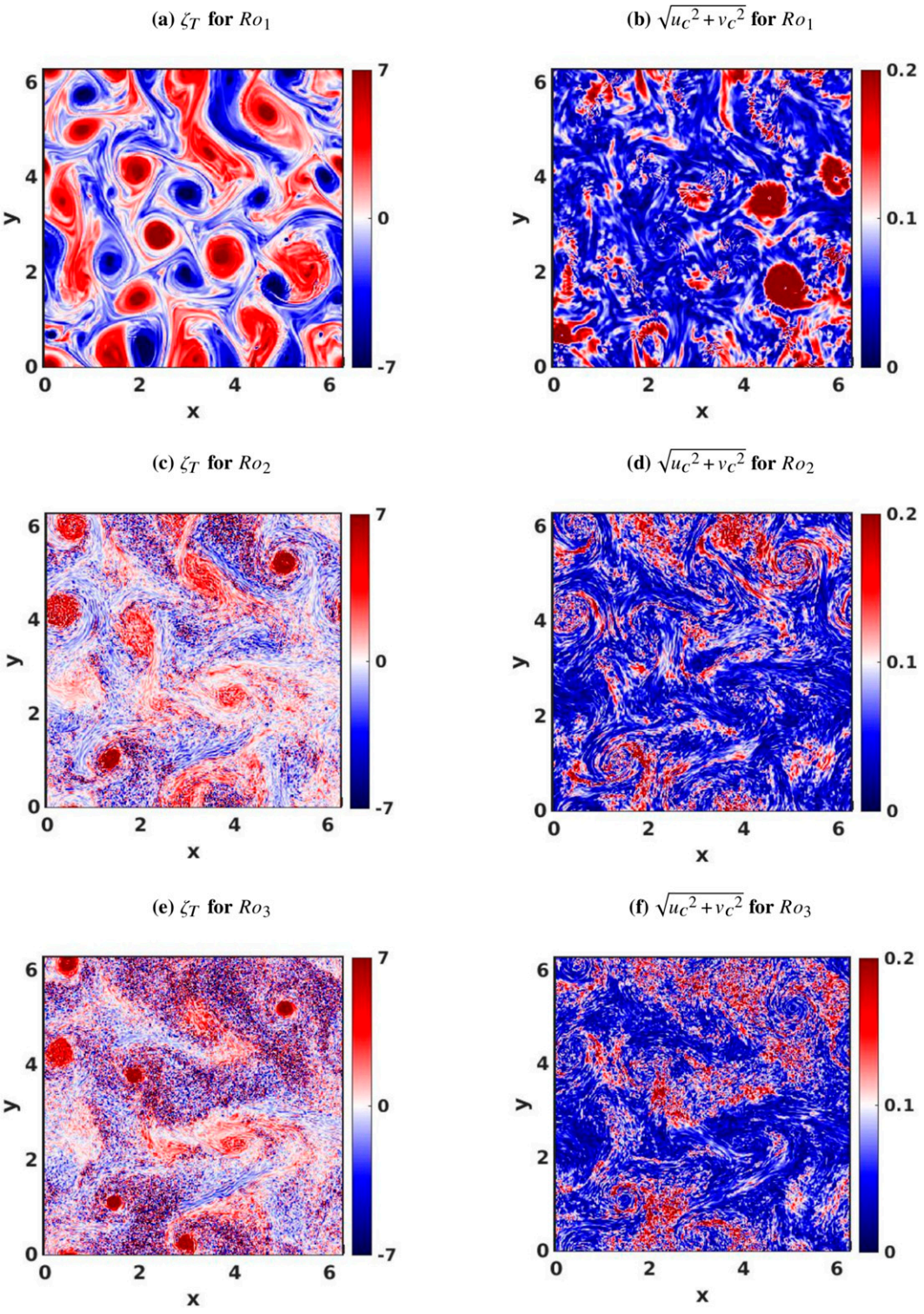

FIG. 1. (left) Barotropic vorticity and (right) baroclinic speed for three different Rossby numbers. Rossby number increases from top to bottom.

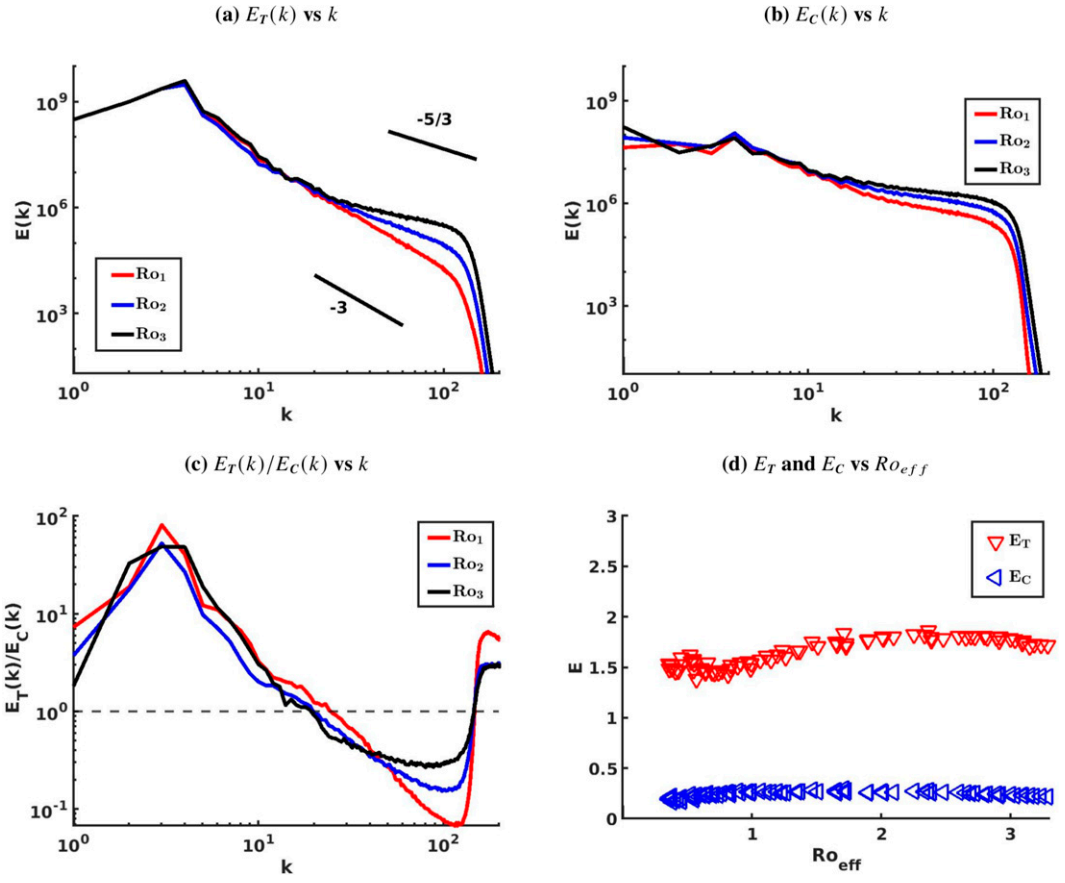

FIG. 2. Energy spectrum of (a) barotropic flow and (b) baroclinic flow for three different Rossby numbers. (c) Ratio of barotropic to baroclinic energy ratio across wavenumbers. (d) Total barotropic (red) and total baroclinic (blue) energy as a function of Rossby number.

by the dispersion relationship of inertia–gravity waves, $\omega(k) = \sqrt{1 + \mathrm{Bu}k^2}$ In contrast, high Rossby number wave component was seen to depart from the linear wave dispersion relationship, implying that even though the linear wave-balance decomposition provides us with a "wave" component, that component do not correspond to linear inertia–gravity waves. These details point out that separating fast linear waves from slow balanced mode using the linear decomposition breaks down at high Rossby numbers. Overall, despite the baroclinic flow being energetically weak and its energy levels not changing appreciably on increasing Rossby number, the nature of the flow changes from being a separable mixture of fast waves and a slow balanced component at low Rossby numbers to a high-frequency inseparable mixture of balance and waves in the $O(1)$ Rossby limit.

Returning to the flow features in physical space, oceanic observations of submesoscale dynamics typically find a pronounced cyclone–anticyclone asymmetry, with a dominance of cyclonic vorticity structures (Rudnick 2001; Shcherbina et al. 2013; Buckingham 2016). This feature is qualitatively seen in the left column of Fig. 1. The lowest Rossby number flow shown in Fig. 1a is composed of more or less the same number of cyclonic and anticyclonic vortices. In contrast, on closely examining Figs. 1c and 1e, smaller-scale cyclonic coherent vortices (red color) are seen to float in an incoherent soup of anticyclonic (blue color) vorticity regions. Although the size of cyclonic coherent vortices decreases with increasing Rossby number, cyclonic vortices remain rugged and persist while anticyclonic coherent vortices start disappearing with increasing Rossby number. Figure 4a quantifies the difference between cyclonic and anticyclonic vorticity structures based on the kurtosis. We divided the domain into positive and negative vorticity regions and computed the kurtosis for both positive and negative vorticity regions separately based on the expression (McWilliams 1984; Remmel and Smith 2009):

$$\mathrm{Kurt} = \frac{\langle \zeta_T^4 \rangle}{(\langle \zeta_T^2 \rangle)^2}, \tag{3}$$

where angle brackets above denote integrating over the domain. Kurtosis is in general higher for flows with coherent structures when compared with flows that have no coherent structures (McWilliams 1984). In Fig. 4a, notice that on moving from low to high Rossby numbers, red markers keep moving above blue markers, indicating that cyclonic vortices have higher kurtosis and remain more coherent in comparison to anticyclonic vortices that have relatively lower kurtosis values

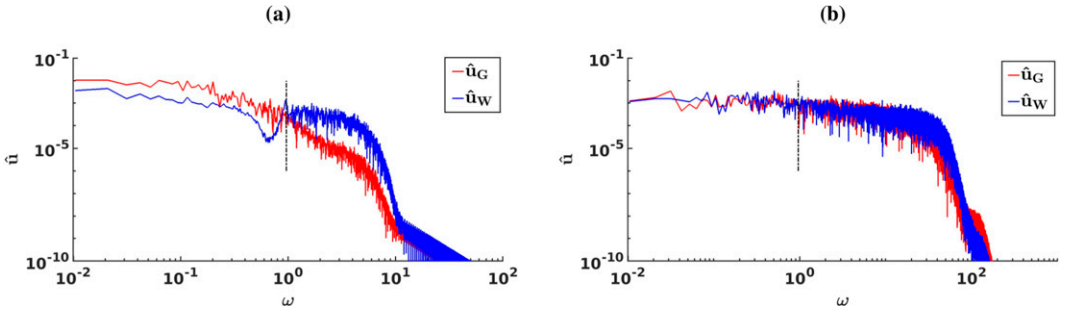

FIG. 3. Frequency spectrum of wave (blue) and balanced (red) fields for the (a) lowest Ro_{eff} and (b) highest Ro_{eff}.

and become incoherent. To further highlight the differences in positive–negative vorticity distributions on increasing Rossby number, Fig. 4b shows histograms of barotropic vorticity for three different Rossby numbers. To make the comparison between different Rossby number cases straightforward, we normalized the frequencies by the maximum frequency for each case, so that the highest frequency of the histogram is 1 for each case (notice that all three histograms meet at 1 on the y axis). While the vorticity field is symmetric at the lowest Rossby number case indicated by the red curve, the histograms become asymmetric at higher Rossby numbers. The skewness of the vorticity fields was seen to monotonically increase with Rossby number as 0.002, 0.06, and 0.15, with the vorticity field being least skewed at the lowest Rossby number case and maximum skewed at the highest Rossby number case. On examining Fig. 4b it can be inferred that for all three cases the high-frequency, low-vorticity parts are more or less symmetric, implying that the weak background vorticity field, in which strong isolated vorticity structures float, exhibit less asymmetry. In contrast, the low-frequency tails of the histograms in Fig. 4b, exhibit a high level of asymmetry. It is seen that the extreme values of positive vorticity are almost double the extreme values of negative vorticity for the highest Rossby number case (black curve). These extreme values primarily correspond to spatially intermittent cyclonic coherent vortices seen in the left panel of Fig. 1. Therefore, with increasing Rossby number, cyclonic vortices remain coherent and take up higher vorticity values while anticyclonic vortices lose coherence and remain in the background with relatively lower extreme vorticity values.

Our analysis so far examined the properties of barotropic and baroclinic flows separately. To see the interconnection between the two flows, we will now examine the spatial correlation between barotropic and baroclinic fields. For this we

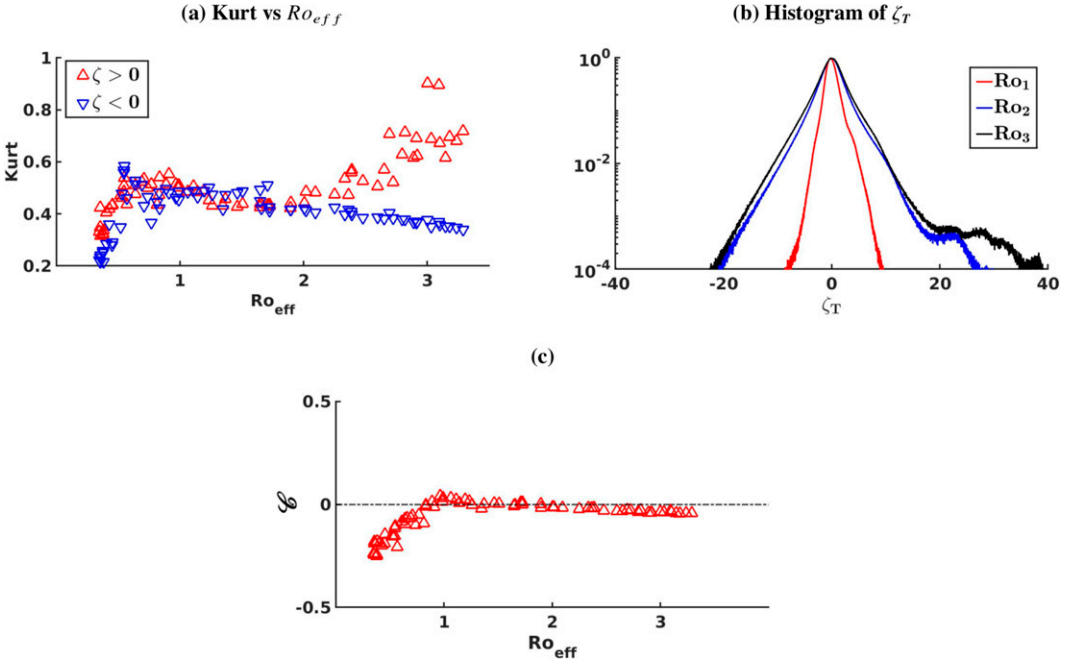

FIG. 4. (a) Kurtosis of cyclonic (red) and anticyclonic (blue) barotropic vorticity. (b) Histogram of barotropic vorticity ζ_T for three different Rossby numbers. (c) Spatial correlation between barotropic and baroclinic flows based on Eq. (5).

computed the correlation between the pointwise baroclinic energy

$$e_C = \frac{\mathbf{v}_C^2}{2} + \mathrm{Bu}\frac{p_C^2}{2} \tag{4}$$

and the barotropic vorticity ζ_T as

$$\mathscr{C} = \frac{\langle \zeta_T e_C \rangle}{\sqrt{\langle \zeta_T^2 \rangle \langle e_C^2 \rangle}}. \tag{5}$$

The above correlation coefficient is plotted in Fig. 4c as a function of Rossby number. Observe that at low Rossby numbers the correlation is negative, indicating that baroclinic energy has an affinity for anticyclonic vortices. This feature can be seen on comparing the physical structures in Figs. 1a and 1b. Notice that the big red patches of baroclinic flow seen in Fig. 1b corresponds to anticyclonic (blue regions) in Fig. 1a. As seen in Fig. 4c, on increasing Rossby number the correlation coefficient moves closer to 0. At high Rossby numbers, as discussed above, anticyclonic vortices are destroyed, resulting in no clear correlation between anticyclonic barotropic vortices and baroclinic flow fields.

a. Spectral fluxes of barotropic and baroclinic modes

We will now examine energy transfers across scales for the barotropic and baroclinic fields. Applying a Fourier transform to the governing equations (1) and manipulating the resulting equations gives us energy equations for barotropic and baroclinic fields at each wavenumber k [see the procedure described in Thomas and Yamada (2019), for example]. Summing the equations so obtained from the maximum resolved wavenumber $k_{\max}$ to an arbitrary wavenumber k gives the energy flux equations for the barotropic and baroclinic flow as

$$\frac{\partial \hat{E}_T(k,t)}{\partial t} = \underbrace{\Pi_{\mathrm{TTT}}(k,t) + \Pi_{\mathrm{TCC}}(k,t)}_{\Pi_T} + \hat{F}_T(k,t) - \hat{D}_T(k,t), \tag{6a}$$

$$\frac{\partial \hat{E}_C(k,t)}{\partial t} = \Pi_C(k,t) + \hat{F}_C(k,t) - \hat{D}_C(k,t). \tag{6b}$$

In the above equations, $\hat{E}_T(k,t)$ and $\hat{E}_C(k,t)$ are barotropic and baroclinic energies contained in the wavenumber band $(k, k_{\max})$, while $\hat{F}_T$ and $\hat{F}_C$ are the forcing, and $\hat{D}_T$ and $\hat{D}_C$ represent the dissipation contained in the same wavenumber band. The barotropic flux above is represented by Π_T while the baroclinic flux is denoted by Π_C. The barotropic flux is further divided into two parts: a part that is due to triadic barotropic interactions alone (Π_{TTT}) and a part that is due to joint barotropic–baroclinic triads (Π_{TCC}).

The flux terms given in (6) are shown in Fig. 5 for the same three Rossby numbers explored earlier. The barotropic flux Π_T shown in Fig. 5a reveals that the magnitude of the flux increases with increasing Rossby number. At low wavenumbers the flux is negative, while in the inertial range, $k \in (10, 100)$, it is positive. Positive barotropic flux in the inertial range implies that the barotropic energy is being transferred downscale, eventually getting dissipated. Furthermore, from Fig. 5a it is clear that the forward flux increases with Rossby number, with the flux being weakest in the inertial range for Ro_1 (red curve) and being the strongest for the highest Rossby number case Ro_3 (black curve). Consequently, on moving from top to bottom in the left column of Fig. 1, the generation of small-scale features in the barotropic flow and shrinking in size of coherent vortices goes hand in hand with an increasingly strong forward flux of barotropic energy.

To explore the barotropic flux in more detail, the two components of the barotropic flux given in Eq. (6a), Π_{TTT} and Π_{TCC} are plotted in Figs. 5b and 5c, respectively. Notice that although the barotropic flux is constant and is represented by a straight line in the inertial range in Fig. 5a, its constituents Π_{TTT} and Π_{TCC} exhibit a certain level of variability in the inertial range. Figure 5b shows that Π_{TTT} is negative, primarily at low wavenumbers, in addition to taking slightly negative values in the inertial range. Additionally, the Π_{TTT} flux component does not change appreciably with increasing Rossby number. The triadic barotropic interactions therefore assist in the upscale transfer of barotropic energy, with rates that are more or less comparable at different Rossby numbers. In contrast to the Π_{TTT} component, the Π_{TCC} flux component shown in Fig. 5c is positive throughout the inertial range, with magnitude increasing with Rossby number. Π_{TCC} is negligible at the lowest Rossby number case (red curve) and reaches largest value at the highest Rossby number case (black curve). Since the Π_{TTT} component is insignificant in the inertial range, as seen in Fig. 5b, the positive flux value in the inertial range seen in Π_T in Fig. 5a is entirely due to the Π_{TCC} flux component. Therefore, although the baroclinic energy is much less than the barotropic energy across different Rossby numbers, the baroclinic flow plays the dominant role in facilitating the forward energy flux of the barotropic flow.

In addition to the Π_{TCC} flux component being positive in the inertial range, as can be seen in Fig. 5c, Π_{TCC} is negative at low wavenumbers. Notice that Π_{TTT} goes to zero at the lowest wavenumber in Fig. 5b, while Π_{TCC} in Fig. 5c does not. This implies that the baroclinic flow, in addition to catalyzing the forward flux of barotropic energy, also extracts some of the barotropic energy. The energy transfer from barotropic to baroclinic mode is extremely small at low Rossby number (notice that the red curve in Fig. 5c meets the y axis at a value slightly below zero) but increases monotonically with increasing Rossby number. Since in our numeral integrations we forced the inertial oscillation mode of the baroclinic flow, the baroclinic flow is energized through two separate sources: direct forcing and energy transfer from barotropic flow. Along the same lines, the barotropic flow loses its energy by two means: energy loss to the baroclinic flow and small-scale dissipation at viscous scales. Since the energy transfer from barotropic to baroclinic mode is a transfer from a low to a high vertical wavenumber mode, this transfer is essentially a forward energy flux in the vertical wavenumber space restricted to two wavenumbers within our idealized setup.

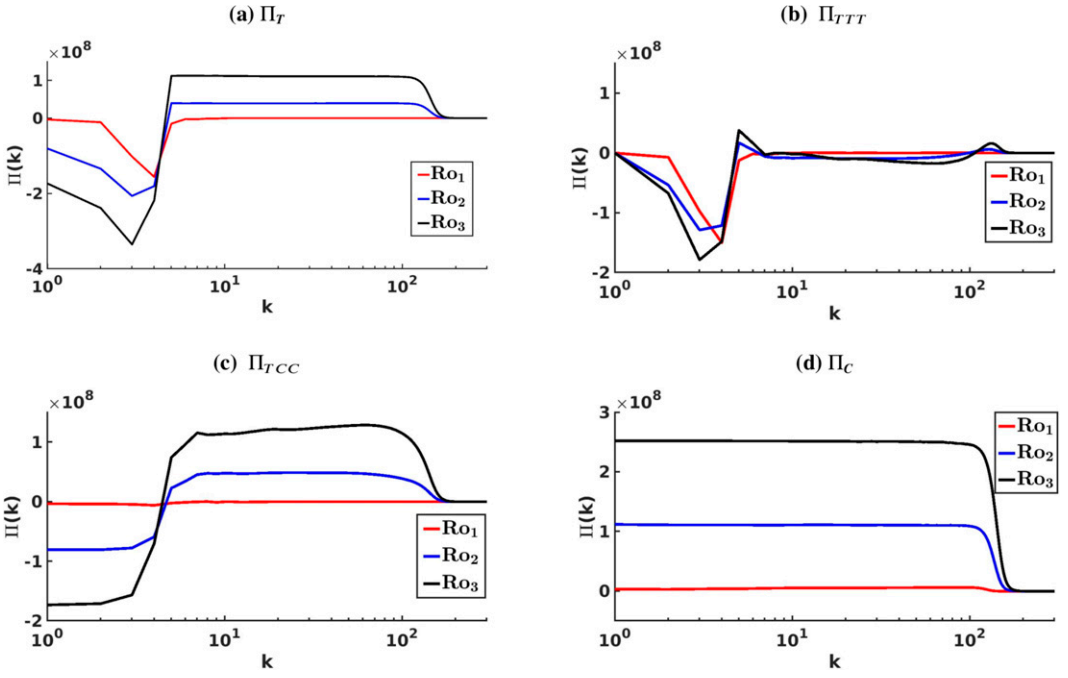

FIG. 5. (a) The barotropic flux Π_T and its decomposition into two components, (b) Π_{TTT} and (c) Π_{TCC}. (d) Baroclinic flux Π_C. Fluxes are shown for three different Rossby numbers. The red curves, corresponding to the lowest Rossby number, have the least flux while the black curves, corresponding to the highest Rossby number, have the largest flux.

Complementary to the barotropic flux, Fig. 5d shows the baroclinic energy flux Π_C for three different Rossby numbers. Π_C is seen to be positive and constant in the inertial range, with magnitude increasing with Rossby number. The baroclinic flow, just like the barotropic flow, undergoes a forward energy flux whose strength monotonically increases with Rossby number. Additionally, as can be seen in Fig. 5d, Π_C is positive at the lowest wavenumber, since as explained earlier, the baroclinic flow is fed through direct forcing and energy transfer from the barotropic flow. Therefore, the baroclinic flow, fed through two different means, fluxes energy down scale and dissipates at the viscous scales; the strength of the process increasing with increasing Rossby number and being accompanied by the generation of finer-scale features in the baroclinic flow seen in the right column of Fig. 1.

b. *Flux distribution in physical space*

The spectral fluxes examined above clarifies energy transfer across scales for the flow. At higher Rossby numbers both barotropic and baroclinic flow fluxes energy downscale and the forward energy flux becomes stronger with increasing Rossby number. Despite spectral fluxes revealing vital information regarding energy transfers across scales, it is still unclear where in physical space the downscale energy transfers take place. For instance, gleaning from top to bottom of Fig. 1 that shows shrinking barotropic coherent vortices and generation of finer-scale features in the flow, it would be beneficial to understand the spatial structure of the forward energy flux with regard to the locations of the coherent vortices.

To identify locations where the forward energy flux of the flow dominates, we will now construct the energy flux equation in physical space. For this we applied a high-pass wavenumber filter on the flow fields. We define filtered variable $\tilde{\psi}(\mathbf{x},\tilde{k})$ as the streamfunction field restricted to scales greater than or equal to a cutoff scale $\tilde{L} = 2\pi/\tilde{k}$. The $\tilde{\psi}$ is therefore obtained by a spectral filter that removes all components of the ψ that are larger than the cut off scale $\tilde{L}$ or wavenumbers lower than $\tilde{k}$, i.e., $\tilde{\psi} = \mathcal{F}^{-1}[\hat{\psi}(k \geq \tilde{k})]$, where $\hat{\psi}$ is the Fourier transform of ψ, and $\mathcal{F}^{-1}$ denotes the inverse Fourier transform. We apply the spectral filter to the governing equations (1) to get

$$\frac{\partial \tilde{\zeta}_T}{\partial t} + \mathrm{Ro}\nabla \times [\widetilde{\mathbf{v}_T \cdot \nabla \mathbf{v}_T} + \widetilde{\mathbf{v}_C \cdot \nabla \mathbf{v}_C} + \widetilde{(\nabla \cdot \mathbf{v}_C)\mathbf{v}_C}] = \tilde{f}_T - \nu\Delta^8 \tilde{\zeta}_T, \tag{7a}$$

$$\frac{\partial \tilde{\mathbf{v}}_C}{\partial t} + \hat{\mathbf{z}} \times \tilde{\mathbf{v}}_C + \mathrm{Bu}\nabla \tilde{p}_C + \mathrm{Ro}(\widetilde{\mathbf{v}_T \cdot \nabla \mathbf{v}_C} + \widetilde{\mathbf{v}_C \cdot \nabla \mathbf{v}_T}) = \tilde{\mathbf{f}}_C - \nu\Delta^8 \tilde{\mathbf{v}}_C, \tag{7b}$$

$$\frac{\partial \tilde{p}_C}{\partial t} + \nabla \cdot \tilde{\mathbf{v}}_C + \mathrm{Ro}\ \widetilde{\mathbf{v}_T \cdot \nabla p_C} = -\nu\Delta^8 \tilde{p}_C. \tag{7c}$$

Above equations govern the evolution of flow variables constrained to scales smaller than $\tilde{L}$. To get energy equation of the flow for scales smaller than $\tilde{L}$, we multiply (7a) by $-\tilde{\psi}_T$, dot (7b) with $\tilde{\mathbf{v}}_C$, multiply (7c) with $\tilde{p}_C$, and sum them up. After manipulating the terms by moving derivatives around, we get

$$\frac{\partial}{\partial t}\left(\frac{1}{2}\tilde{\mathbf{v}}_T^2+\frac{1}{2}\tilde{\mathbf{v}}_C^2+\frac{1}{2}\mathrm{Bu}\,\tilde{p}_C^2\right)=\nabla\cdot\mathbf{M}_1+\nabla\times\mathbf{M}_2+\nabla\cdot\mathbf{M}_3+\tilde{\Pi}_T+\tilde{\Pi}_C+\tilde{F}-\tilde{D},\tag{8}$$

where

$$\mathbf{M}_1=-\mathrm{Bu}\,\tilde{p}_C\tilde{\mathbf{v}}_C+\tilde{\psi}_T\nabla\frac{\partial\tilde{\psi}_T}{\partial t},\tag{9a}$$

$$\mathbf{M}_2=\mathrm{Ro}\,\tilde{\psi}_T[\widetilde{\mathbf{v}_T\cdot\nabla\mathbf{v}_T}+\widetilde{\mathbf{v}_C\cdot\nabla\mathbf{v}_C}+\widetilde{(\nabla\cdot\mathbf{v}_C)\mathbf{v}_C}],\tag{9b}$$

$$\mathbf{M}_3=-\mathrm{Ro}[\tilde{v}_{Ti}(\widetilde{v_{Ti}\mathbf{v}_T}+\widetilde{v_{Ci}\mathbf{v}_C})+\tilde{v}_{Ci}(\widetilde{v_{Ti}\mathbf{v}_C}+\widetilde{v_{Ci}\mathbf{v}_T})+\mathrm{Bu}\,\tilde{p}_C\widetilde{(p_C\mathbf{v}_T)}],\tag{9c}$$

$$\tilde{\Pi}_T=\mathrm{Ro}\frac{1}{2}\left(\frac{\partial\tilde{v}_{Ti}}{\partial x_k}+\frac{\partial\tilde{v}_{Tk}}{\partial x_i}\right)\widetilde{v_{Ti}v_{Tk}},\tag{9d}$$

$$\tilde{\Pi}_C=\mathrm{Ro}\frac{1}{2}\left(\frac{\partial\tilde{v}_{Ti}}{\partial x_k}+\frac{\partial\tilde{v}_{Tk}}{\partial x_i}\right)\widetilde{v_{Ci}v_{Ck}}+\mathrm{Ro}\frac{1}{2}\left(\frac{\partial\tilde{v}_{Ci}}{\partial x_k}+\frac{\partial\tilde{v}_{Ck}}{\partial x_i}\right)\times(\widetilde{v_{Ti}v_{Ck}}+\widetilde{v_{Ci}v_{Tk}})+\mathrm{Ro}\,\widetilde{v_{Ci}}\widetilde{\left(v_{Ti}\frac{\partial v_{Ck}}{\partial x_k}\right)}+\mathrm{RoBu}\,(\widetilde{p_Cv_{Tk}})\frac{\widetilde{\partial p_C}}{\partial x_k}.\tag{9e}$$

For convenience we used the index notation in the expressions in (9), with v_i being the ith component of the vector $\mathbf{v}$ and repeated indices imply summation over that index.

In Eq. (8), the left-hand side is the rate of change of flow energy contained in scales equal to and smaller than $\tilde{L}$ and the right-hand side contains terms responsible for the change, which are expanded in (9) [we refer readers not acquainted with equations like (8) to chapter 13 of Pope (2000) for derivation of similar equations via filtering]. Integrating (8) over the entire domain, the left-hand side becomes the time rate of change of total energy contained in scales smaller than $\tilde{L}$, while the first three terms on the right-hand side vanish since they contain divergence and curl of vectors. Barring the contribution from the forcing and dissipation [expressed by the last two terms of (8)], the fourth and fifth terms on the right-hand side of (8)— $\tilde{\Pi}_T$ and $\tilde{\Pi}_C$ —are the terms responsible for transferring energy across scales. It is important to keep in mind that (8) captures the rate of change of total flow energy. Consequently, $\tilde{\Pi}_T+\tilde{\Pi}_C$ in (8) represents the total flow energy flux in physical space, with $\tilde{\Pi}_T$ being flux contribution to the barotropic component alone while $\tilde{\Pi}_C$ is the flux contribution involving both barotropic and baroclinic modes. Equation (8) therefore is equivalent to the physical space representation of the sum of the barotropic and baroclinic energy flux equations given in (6). We examined $\tilde{\Pi}_T$ and $\tilde{\Pi}_C$ across the inertial range for different Rossby numbers. At all Rossby numbers, the energy flux involving barotropic modes alone, $\tilde{\Pi}_T$, was seen to be small in magnitude and negative in sign, implying that the barotropic modes by themselves were inducing a weak inverse energy flux of the flow. In contrast, the energy flux involving baroclinic flow, $\tilde{\Pi}_C$, was seen to be positive in sign with its magnitude increasing monotonically with Rossby number. These inferences are qualitatively similar to those inferred from spectral space transfers based on Fig. 5, i.e., the barotropic triads induce a weak inverse energy flux while the flux involving the baroclinic term induces a forward energy flux whose strength increases monotonically with Rossby number. We will therefore take a closer look at the spatial structure of $\tilde{\Pi}_C$, this being the specific flux term that is responsible for the forward flux of the flow energy.

For the broad set of Rossby number flows discussed earlier, we examined $\tilde{\Pi}_C$ by choosing different filter wavenumber $\tilde{k}$ (or filter scale $\tilde{L}$). A specific example of the spatial structure of the flux is given in Fig. 6a, where $\tilde{\Pi}_C$ normalized by its spatially integrated value, $\langle\tilde{\Pi}_C\rangle$, is shown for the highest Rossby number flow, Ro_3, with the filter wavenumber $\tilde{k}=40$ (as can be seen from the energy spectra shown in Fig. 2, this corresponds to the middle of the inertial range, sufficiently far from forcing and dissipative scales). Observe in Fig. 6a that the flux is spatially intermittent and patchy, taking up both positive and negative values in physical space. Furthermore, as can be gleaned from the histogram of the flux shown in Fig. 6b, extreme values of flux (positive and negative) have low frequency. Nevertheless, from Fig. 6b it can be seen that the extreme positive values of flux are more frequent than extreme negative values of flux (notice that the black curve on the positive side goes up to 2 on the x axis, while the curve falls off rapidly well before -2). This skewed flux with higher positive flux values in the domain results in the net flux integrated over the domain being positive, i.e., $\langle\tilde{\Pi}_C\rangle>0$, indicating that the flow energy is transferred from large to small scales.

To get a handle on regions in physical space where the flow energy is fluxed downscale, we partitioned the flow domain into different regions based on the Okubo–Weiss criterion (Okubo 1970; Weiss 1991), this decomposition being commonly used in the oceanography (Shcherbina et al. 2013; Chelton et al. 2007; Isern-Fontanet et al. 2006). For a flow velocity field (u, v), if we define the normal strain rate as $\sigma_n=\partial u/\partial x-\partial v/\partial y$ and shear strain rate as $\sigma_s=\partial v/\partial x+\partial u/\partial y$, the total strain rate is $\sigma=\sqrt{\sigma_n^2+\sigma_s^2}$. Based on flow vorticity $\zeta=\partial v/\partial x-\partial u/\partial y$, we may partition the flow domain as strain-dominant regions, $\sigma>|\zeta|$, and vorticity-dominant regions, $\sigma<|\zeta|$. Since the number of points that satisfied the exact equality $\sigma=|\zeta|$ were insignificantly small, we ignored such points to keep strict inequalities $\sigma>|\zeta|$ and $\sigma<|\zeta|$.

For the highest Rossby number flow, Figs. 6c and 6d shows the spatial structure of total strain rate and vorticity of the barotropic flow, respectively, computed at the same instant at which the flux in Fig. 6a was computed. On comparing the strain and vorticity fields shown in Figs. 6c and 6d, it can be seen that strain takes up extremely large values in vortex peripheries, regions outside vortex cores. In contrast, vortex cores, seen with "holes" in Fig. 6c, are regions where strain is weak and vorticity dominates. Of course, as can be seen from Figs. 6c and 6d, strain rate and vorticity field do take up sparse high values away from vortex structures, implying that there are small, localized regions located away from vortices where strain rate dominates over vorticity and vice versa. Nevertheless, on comparing pointwise strain rate and vorticity field at different

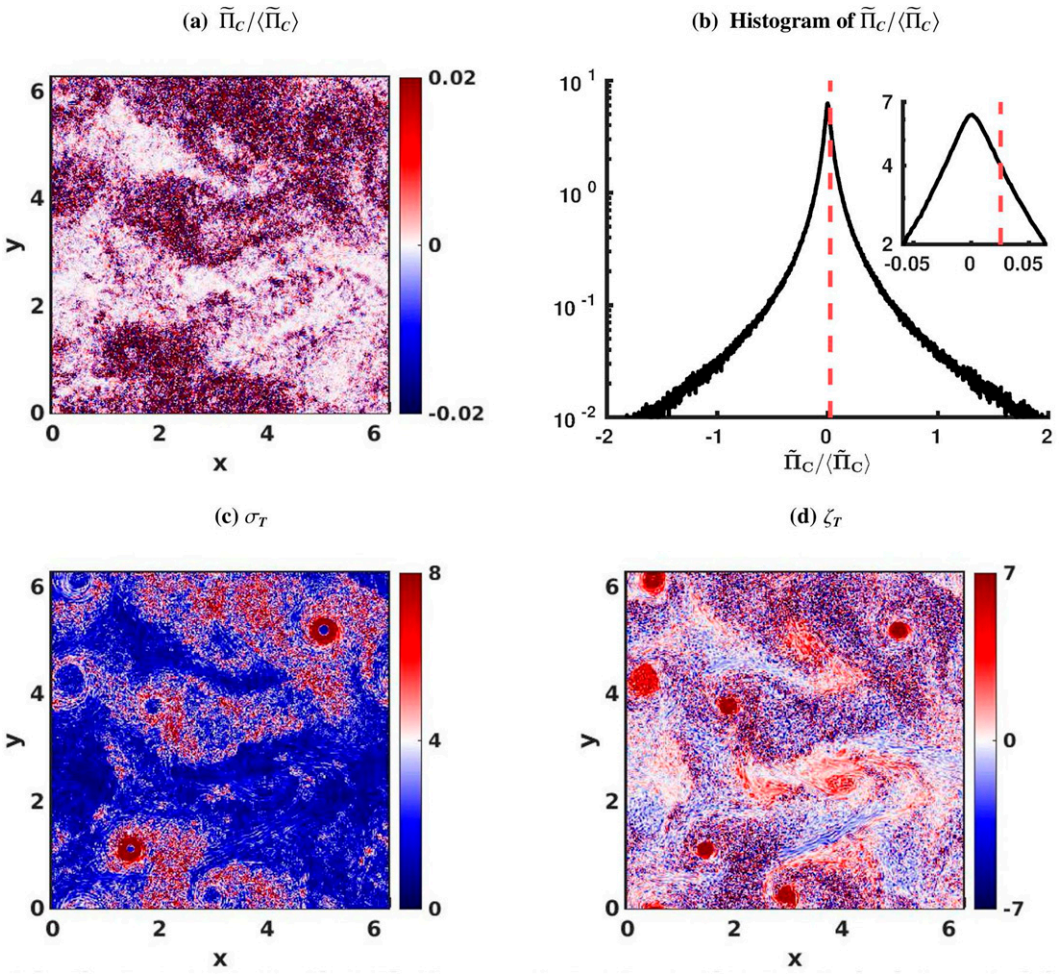

FIG. 6. (a) Spatial structure of normalized flux $\tilde{\Pi}_C/\langle\tilde{\Pi}_C\rangle$. (b) Histogram of $\tilde{\Pi}_C/\langle\tilde{\Pi}_C\rangle$, corresponding to the flux shown in (a). The red dashed line indicates the mean of the normalized flux. The inset shows a smaller part of the histogram, highlighting the mean of the normalized flux. (c) Spatial structure of barotropic strain rate σ_T. (d) Spatial structure of barotropic vorticity ζ_T. Panel (d) is the same as Fig. 1e, shown here for easier comparison between spatial structure of vorticity, strain rate, and flux.

times, above observation was seen to be a generic feature. A significant portion of strain-dominant regions ($\sigma_T > |\zeta_T|$) are vortex peripheries while vortex cores are regions of vortex dominance ($\sigma_T < |\zeta_T|$).

To get a grip on the flux distribution in physical space, compare Figs. 6a, 6c, and 6d. Notice that the flux takes up higher values in vortex peripheries, outside vortex cores, where strain rate dominates over vorticity. In fact, on closely staring at Fig. 6a, the reader will notice holes in the flux field, corresponding to physical locations of the vortex cores in Fig. 6d, which are regions that appear as holes in the strain rate shown in Fig. 6c. To quantify flux distribution in physical space based on the strain-vorticity criterion, we spatially integrated $\tilde{\Pi}_C$ constrained to strain-dominant regions ($\sigma_T > |\zeta_T|$) and vorticity-dominant regions ($\sigma_T < |\zeta_T|$) and found that the former accounted for 61.5% of the flux while the latter constituted only 38.5% of the net flux. Therefore, the dominant fraction of the forward energy flux is based on strain-dominant regions, away from vortex cores. Alternatively, vortex cores are regions of minimal net forward energy flux, the coherent structures being shielded from losing their energy to smaller dissipative scales.

The specific quantitative inferences made above are for the highest Rossby number case Ro_3. Nevertheless, the qualitative features described above were robustly seen for other $O(1)$ Rossby number flows as well. On moving from asymptotically small to $O(1)$ Rossby numbers, the forward flux term $\tilde{\Pi}_C$ strengthens and a major fraction of the forward energy flux (generically more than 60%) takes place in strain dominated regions. Since the baroclinic flow plays a key role in the forward energy flux, via the $\tilde{\Pi}_C$ term, it is useful to examine the distribution of the pointwise baroclinic energy e_C with respect to the strain-dominant and vorticity-dominant regions. We therefore computed spatially integrated e_C [see expression in Eq. (4)] constrained on strain-dominant and vorticity-dominant regions. The results shown in Fig. 7a indicate that

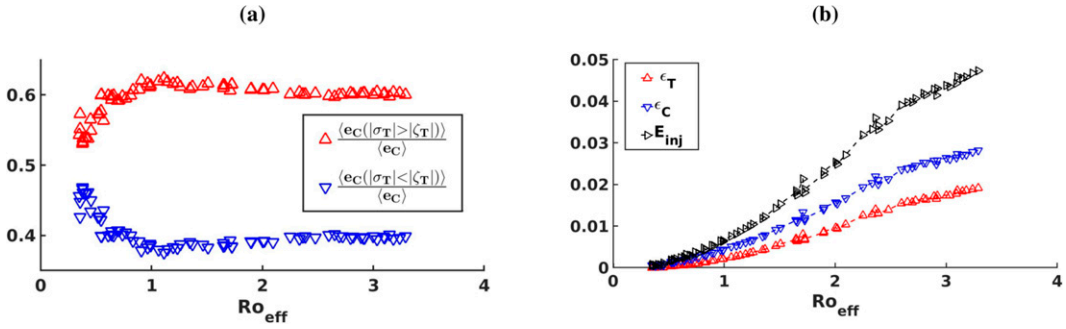

FIG. 7. (a) Fractional baroclinic energy in strain dominated (red) and vorticity dominated (blue) regions. (b) Barotropic dissipation (red), baroclinic dissipation (blue), and total energy injection rate (black).

although at low Rossby numbers the contributions from the two regions are comparable, on increasing Rossby number, a relatively higher level of baroclinic energy is associated with strain-dominant regions in physical space. Recall that at low Rossby numbers the baroclinic flow has an affinity for anticyclonic barotropic vortices (as can be seen in the first row of Fig. 1). At $O(1)$ Rossby numbers, with anticyclonic barotropic vortices being destroyed, higher concentration of baroclinic flow shifts to barotropic strain-dominant regions, outside cyclonic vortex cores (as can be seen in the last row of Fig. 1). On comparing spatial structure of small-scale dissipation, similar to the spatial structure of flux, we found that the major fraction of flow dissipation was in strain-dominant regions, with high dissipation values being observed in vortex peripheries. Therefore, with increasing Rossby number, the baroclinic flow migrates to regions outside vortex cores and strengthens the forward flux of flow energy, disintegrating peripheries of vortices and shrinking size of coherent vortices, as seen in the left column of Fig. 1, thereby enhancing small-scale dissipation in those regions.

At this point we remind the reader that the flux equation (8) is for the total flow energy. Starting from the spatially filtered equations (7), it is straightforward to construct separate flux equations in physical space for the barotropic and baroclinic energy. We examined spatial structure of fluxes for the barotropic and baroclinic energy based on such equations (figures omitted) and found details similar to that mentioned above and gleaned from Fig. 6. The forward energy fluxes of both barotropic and baroclinic flow are generically dominant in regions where barotropic strain rate dominates over barotropic vorticity, these being regions where baroclinic energy levels are high.

Much of the detailed diagnosis described above requires high-resolution spatiotemporal data that are difficult to obtain from typical oceanic observational campaigns. Nevertheless, Yang et al. (2017) is a recent work that compares properties of the flow in eddy core and eddy periphery regions with an eye on submesoscale dynamics. On exploring properties of multiple coherent eddies in South China Sea, they found that small-scale features (shallower energy spectrum), forward energy flux, and small-scale mixing was much more enhanced in eddy peripheries when compared with eddy core regions. While the sparse datasets they had access to prevented more detailed diagnosis, the key inferences of Yang et al. are qualitatively similar to our findings discussed above. That is, the eddy peripheries are regions of higher concentration of energetic small-scale flow structures, stronger forward energy flux, and enhanced small-scale dissipation when compared to eddy core regions.

c. *Monotonic increase in small-scale dissipation*

Returning to the spectral fluxes shown in Figs. 5a and 5d, notice that the barotropic and baroclinic forward flux in the inertial range increases with increasing Rossby number, suggesting that higher amounts of energy are flowing through the system. To confirm this, Fig. 7b plots barotropic dissipation, baroclinic dissipation, and total energy injection rate. The total energy injection rate is the sum of energy injection rate into the barotropic and baroclinic modes and is equal to the sum of barotropic and baroclinic dissipation in forced-dissipative equilibrium. As mentioned earlier, the baroclinic flow is energized through direct external forcing and energy transfer from the barotropic flow, due to which baroclinic dissipation (blue curve) is more than barotropic dissipation (red curve) in Fig. 7b. Observe the monotonic increase in all three quantities with increasing Rossby number in Fig. 7b. We remind the reader once again that our forcing scheme does not impose a fixed rate of energy injection; energy at large scales are forced and maintained, and the system decides the energy flow rate through the system at different Rossby numbers. Given this, it is interesting that larger and larger amount of energy flows through the system with increasing Rossby number. More striking is this result in comparison to the result seen in Fig. 2d: although more and more energy flows through the system, the energy levels of barotropic and baroclinic modes do not change appreciably. The increased drawing of energy into the system is compensated by increased dissipation at small scales, resulting in more or less same flow energy levels at different Rossby numbers.

4. Summary and perspectives

Oceanic flows typically contain a major fraction of their energy in low vertical modes, while various forms of external perturbations can generate low-energy, high-baroclinic flow disturbances. Although the high-baroclinic disturbances may have low energy levels, the interaction between the low and

high modes may be weak or strong depending on the flow Rossby number. To investigate energetic interactions and turbulent flow dynamics of an $O(1)$ flow being capable of sustaining large-scale coherent structures with a weak high mode disturbance across different Rossby numbers, we idealized the interaction problem by restricting the flow components to an energetic barotropic mode and a single low-energy, high-baroclinic mode. Ignoring inertia–gravity waves and other ageostrophic components, two-vertical-mode models have been extensively used in the past in connection to geostrophic turbulence (Salmon 1998; Larichev and Held 1995). As an extension, recent works have used such reduced models to explore how inertia–gravity waves modify geostrophic turbulence in the small Rossby number regime (Thomas and Yamada 2019; Thomas and Arun 2020). Inspired by observations of energetic submesoscale flows with $O(1)$ Rossby numbers in the ocean, in the present work we explored the changes in flow structures and energy flow pathways as Rossby number was gradually increased from asymptotically small to $O(1)$ values.

To set up the flow at different Rossby numbers, we used a specialized setup where large-scale flow energy was forced and maintained to be a constant. The large-scale barotropic flow, at wavenumbers $k \leq 5$, was maintained to have unit energy while the spatially homogeneous inertial oscillation mode of the baroclinic flow was forced and maintained at an energy 0.1. Using such a setup ensured that we did not impose a fixed energy injection rate on the system; rather we let the system choose the energy injection rate based on the energy flow rate through the system at different Rossby numbers. We then numerically integrated the governing equations to generate 77 flows in forced-dissipative equilibrium, with Rossby number varying from asymptotically small values to $O(1)$ values.

The inertial oscillation mode of the baroclinic flow, which was externally forced and maintained, interacted with the barotropic flow and generated a spatially inhomogeneous baroclinic flow field at all Rossby numbers. At low Rossby numbers, the barotropic flow exhibited an inverse energy flux and organized itself into large-scale coherent vortices while the baroclinic flow fluxed energy downscale. The baroclinic flow was also seen to be concentrated in anticyclonic barotropic vortices. The barotropic flow modified the dynamics of the baroclinic flow, along with a weak barotropic to baroclinic energy transfer. In contrast, with increasing Rossby numbers, the barotropic and baroclinic flow were rich with energetic small-scale structures, shallower energy spectra, and forward energy flux.

At low Rossby numbers, we observed symmetric distribution of cyclonic and anticyclonic vorticity structures of the barotropic flow. In contrast, $O(1)$ Rossby number flows were characterized by highly asymmetric barotropic vorticity distribution with a dominance of cyclonic vortices over anticyclonic ones. The barotropic coherent vortices at $O(1)$ Rossby numbers were seen to be fewer in number and smaller in size. Additionally, barotropic to baroclinic energy transfer was seen to increase monotonically with Rossby number. The $O(1)$ Rossby number flows were in general characterized by a forward energy flux for both the barotropic and baroclinic flow and the turbulent energy transfers in the two-vertical-mode system based on our present study is summarized in schematics shown in Fig. 8.

The forward energy flux of the flow was also seen to monotonically increase with increasing Rossby number. On partitioning the domain based on the barotropic flow field into vortex dominant regions, which were mostly regions inside vortex cores, and strain-dominant regions, which consisted of regions in the vortex peripheries, we found that the forward energy flux of the flow was higher in strain-dominant regions, away from vortex cores. Notably, these were also regions where a major fraction of baroclinic flow was seen to be accumulated at high Rossby numbers. Therefore, with increasing Rossby numbers, the forward energy flux of the flow strengthens, with higher net flux in vortex peripheries, which goes hand-in-hand with shrinking size of coherent vortices and increased small-scale dissipation.

As explained earlier, throughout out this work, across different Rossby numbers, we forced and maintained large-scale energy levels of the flow. Such a forcing scheme has no control over how the total barotropic and baroclinic energy levels would change with different Rossby numbers. Nevertheless, we observed that the barotropic and the baroclinic energy levels were not changing appreciably with increasing Rossby number, ensuring that the major fraction of the flow energy was associated with the barotropic flow, while the baroclinic flow was a small perturbation. The low-energy baroclinic flow assisted in generating small-scale barotropic flow features and facilitated the forward flux of the flow energy, the intensity of which increased with increasing Rossby number. Although multiple previous investigations based in idealized setups, realistic ocean models, and in situ observations have found the flow transition with a forward flux and increased small-scale dissipation at submesoscales (Barkan et al. 2017; Taylor and Straub 2016, 2020; Poje et al. 2017; Naveira Garabato et al. 2022), the low amount of unbalanced energy required to trigger the transition is one of the highlights of this study. It is striking that this behavior is contrary to the case in low Rossby numbers, where large-scale coherent vortices remain rugged and persistent unless unbalanced flow energy levels significantly exceed balanced energy (Thomas and Yamada 2019; Thomas and Arun 2020; Thomas and Daniel 2020, 2021). In our present investigation, even though the baroclinic flow remained a small perturbation to the total flow, the baroclinic flow did more and more damage to the barotropic flow with increasing Rossby number.

To fully appreciate the significance of the last line above, it is worth comparing our results with that of Dritschel and Viudez (2006), who integrated the Boussinesq equations enforcing balanced constraints by filtering off unbalanced components of the flow during small time intervals of the numerical integration (a procedure that they call "optimal balance"). By forcibly enforcing balance constraints on the flow, thereby removing the unbalanced energy in the system, they observed that the generic features of balanced flow holds even when Rossby number reaches $O(1)$ values. In other words, balanced flow can be made to retain its features even at high Rossby numbers, if the unbalanced energy levels are

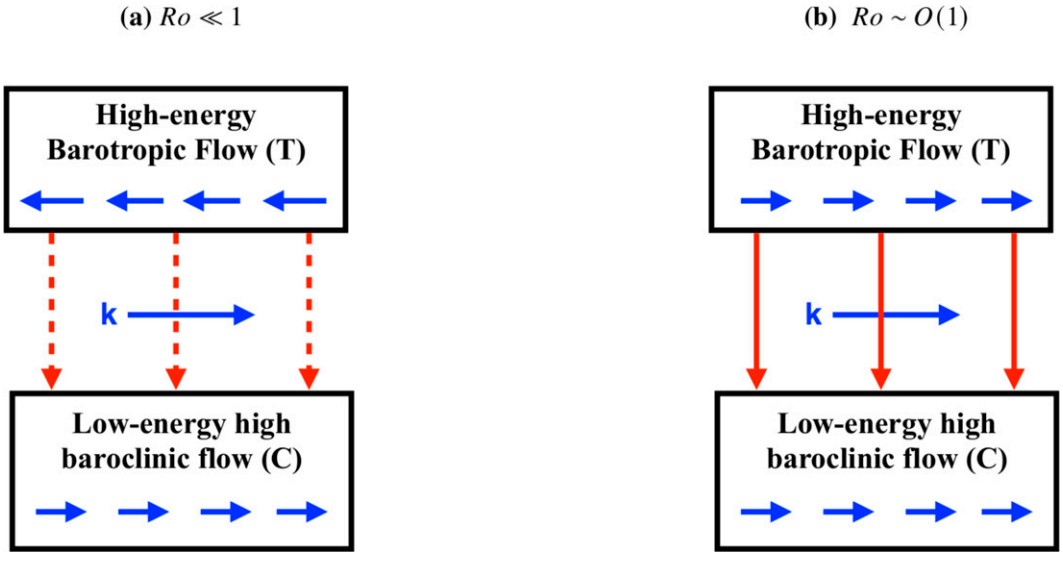

FIG. 8. Schematics of turbulent interactions between (top) a high-energy barotropic flow and (bottom) an energetically weak high-baroclinic flow. The blue arrows indicate energy transfer across scales, with wavenumber (k) increasing from left to right. The red arrows indicate energy transfer between modes. (a) The energy transfers in the low Rossby number regime. The barotropic and baroclinic flows exhibit inverse and forward energy fluxes, respectively, along with a weak energy transfer from barotropic to baroclinic mode as indicated by the dashed red arrows. (b) The turbulent dynamics in the $O(1)$ Rossby number regime. The baroclinic flow extracts significantly more energy from the barotropic flow when compared to the low Rossby number case, as shown by the solid red arrows, undergoes a forward energy flux, and actively catalyzes a forward energy flux of the barotropic flow. Therefore, even though the baroclinic flow is an energetically weak flow component, in $O(1)$ Rossby number regimes it can insinuate a forward barotropic energy flux.

enforced to be zero. To set up a similar experiment in our model, we integrated (1) with Ro = 1, forcibly setting the baroclinic flow to be zero after every few time steps of numerical integration. Figure 9 shows the barotropic vorticity field for such an integration with $\mathrm{Ro_{eff}} = 3.49$: observe the appearance of cyclonic and anticyclonic large-scale coherent vortices. Of course, although our procedure of filtering off baroclinic flow along with time integration is a crude attempt to mimic the more rigorous optimal balance enforcing procedure of Dritschel and Viudez, a comparison between Figs. 9 and 1e drives the main message home: both these flows have similar $O(1)$ Rossby numbers, but the presence of a weak baroclinic flow makes a significant difference when compared to the situation with no baroclinic flow. In $O(1)$ Rossby number flows, even a small unbalanced energy can severely damage the large-scale coherent flow structures.

A reader with interdisciplinary interests will find it intriguing to know that the result mentioned above has similarities with laminar to turbulence transition in pipe flows. Experimental investigations exploring pipe flows have found that the perturbation energy required to trigger transition from laminar to turbulent state decreases proportionally with increasing Reynolds number. Alternatively, the same perturbation magnitude can speed up the transition to turbulence and inflict more damage to the laminar flow at higher Reynolds numbers (Hof et al. 2003; Eckhardt et al. 2007). Although our work was not capturing a laminar to turbulent transition, the transition seen in the barotropic flow in the left column of Fig. 1 is a change from a well-organized flow with most of its energy in large-scale coherent vortices to a flow with relatively higher energy content in incoherent small-scale structures and with a strong forward energy flux. Therefore, although flows in pipe and the flows we investigated in this work in connection to geophysical

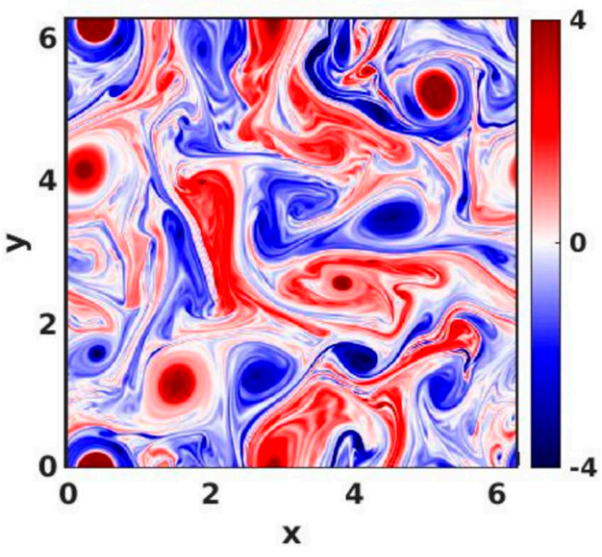

FIG. 9. Barotropic vorticity field with $\mathrm{Ro_{eff}} = 3.49$, obtained by integrating (1) with baroclinic flow forcibly filtered off along with time integration.

turbulence in the ocean are poles apart, we may draw a qualitative analogy between the results in the two setups. The same small, unbalanced perturbation can cause more damage to the flow at higher Rossby numbers in geophysical turbulence and at higher Reynolds numbers in pipe flows.

We conclude by pointing out a specific ramification of the results of our study. Our goal in this paper was to examine how a low-energy high-baroclinic mode, excited on top of an energetic barotropic mode, will affect the flow dynamics across different Rossby numbers. Intriguingly, we found that at $O(1)$ Rossby numbers even low-energy, high-baroclinic flows can induce a forward energy flux and severely enhance dissipation of the flow energy. In the ocean, a wide range of perturbations can generate high-baroclinic mode disturbances. Such unbalanced ageostrophic components, which include inertial oscillations and near-inertial waves, are generated when geostrophic eddies interact with lateral boundaries, topographic features, or as a result of spontaneous emission by high Rossby number vortices and fronts (Liang and Thurnherr 2012; Alford et al. 2013; Clément et al. 2016). From the point of view of loss of balance, balanced coherent structures generating ageostrophic flow components is considered to be a mechanism by which the balanced flow loses energy, the energy being "lost" from balanced flow to the newly excited unbalanced flow component. Despite such mechanisms being hypothesized to be an energy sink for balanced structures, the energy levels of the newly excited imbalance are usually small, compared to the mean or balanced energy. In connection to this, recall that our findings point out that high-baroclinic perturbations in the $O(1)$ Rossby number regime could irreversibly modify coherent vortices and enhance small-scale dissipation. Therefore, in addition to balanced structures' energy loss via the direct generation of unbalanced flow components, the newly generated unbalanced flow could feed back on the balanced structures and could potentially assist in the dissipation of the balanced structures that generated them. In other words, at $O(1)$ Rossby numbers, newly excited unbalanced flow could do more damage to the structures that gave birth to them, than simply being a direct energy sink for the balanced coherent structures. We speculate that this feedback of unbalanced ageostrophic flow could play a role in dissipating balanced flow energy in localized high Rossby flow regions of the world's oceans.

Data availability statement. The datasets used for this work can be downloaded from https://zenodo.org/record/6673261.

APPENDIX

Forcing Scheme

Here we will describe the details of the forcing scheme used to enforce constant energy at large scales of the flow. The forcing scheme on the barotropic flow can be represented in spectral space as

$$\hat{\psi}_k^{(n+1)} = \hat{\psi}_k^{(n)} + a^{(n)}\exp(i\theta_k^{(n)}), \tag{A1}$$

where $a^{(n)}\exp(i\theta_k^{(n)})$ is the forcing term and $\hat{\psi}_k^{(n)}$ and $\hat{\psi}_k^{(n+1)}$ are the streamfunction fields before and after the forcing is implemented. At every iteration the phase $\theta_k^{(n)} \in [0, 2\pi)$ is randomly chosen. Our goal is to find the amplitude $a^{(n)} \in \mathbb{R}$ that will ensure constant energy at large scales. From (A1) we have

$$(k\hat{\psi}_k^{(n+1)*})(k\hat{\psi}_k^{(n+1)}) = [k\hat{\psi}_k^{(n)*} + ka^{(n)}\exp(-i\theta_k^{(n)})] \times [k\hat{\psi}_k^{(n)} + ka^{(n)}\exp(i\theta_k^{(n)})] \tag{A2a}$$

$$\Rightarrow k^2|\hat{\psi}_k^{(n+1)}|^2 = k^2|\hat{\psi}_k^{(n)}|^2 + k^2a^{(n)2} + k^2a^{(n)}\hat{\psi}_k^{n}\exp(-i\theta_k^{(n)}) + k^2a^{(n)}\hat{\psi}_k^{n*}\exp(i\theta_k^{(n)}) \tag{A2b}$$

Above, the * denotes the complex conjugate. We sum the above expression from $k > 0$ to $k = k_f$, since $k \in (0, k_f]$ is the forced band of wavenumbers, to get

$$\sum_{k\in(0,k_f]} k^2|\hat{\psi}_k^{(n+1)}|^2 = \sum_{k\in(0,k_f]} k^2|\hat{\psi}_k^{(n)}|^2 + a^{(n)2}\sum_{k\in(0,k_f]} k^2 + a^{(n)}\sum_{k\in(0,k_f]} k^2[\hat{\psi}_k^{(n)}\exp(-i\theta_k^{(n)}) + \hat{\psi}_k^{(n)*}\exp(i\theta_k^{(n)})]. \tag{A3}$$

The left-hand side term above denotes the barotropic energy in the band $(0, k_f]$ after the forcing scheme is implemented and the first term on the right-hand side above denotes the barotropic energy in the same wavenumber band before the forcing scheme is implemented. These two expressions should be equal to maintain constant total energy in the forced wavenumber band. Equating and canceling these terms and further simplification of (A3) gives us

$$a^{(n)} = -\sum_{k\in(0,k_f]} k^2[\hat{\psi}_k^{(n)}\exp(-i\theta_k^{(n)}) + \hat{\psi}_k^{(n)*}\exp(i\theta_k^{(n)})] \Big/ \sum_{k\in(0,k_f]} k^2. \tag{A4}$$

Above expression gives us the amplitude required in the forcing expression (A1) to maintain constant barotropic energy in the forced wavenumber band $k \in (0, k_f]$. We used the same forcing strategy as above to maintain constant energy in the inertial oscillation mode of the baroclinic flow.

REFERENCES

Alford, M. H., A. Y. Shcherbina, and M. C. Gregg, 2013: Observations of near-inertial internal gravity waves radiating from a frontal jet. *J. Phys. Oceanogr.*, **43**, 1225–1239, https://doi.org/10.1175/JPO-D-12-0146.1.

——, J. MacKinnon, H. Simmons, and J. Nash, 2016: Near-inertial internal gravity waves in the ocean. *Annu. Rev. Mar. Sci.*, **8**, 95–123, https://doi.org/10.1146/annurev-marine-010814-015746.

Barkan, R., K. B. Winters, and J. C. McWilliams, 2017: Stimulated imbalance and the enhancement of eddy kinetic energy dissipation by internal waves. *J. Phys. Oceanogr.*, **47**, 181–198, https://doi.org/10.1175/JPO-D-16-0117.1.

Boccaletti, G., R. Ferrari, and B. Fox-Kemper, 2007: Mixed layer instabilities and restratification. *J. Phys. Oceanogr.*, **37**, 2228–2250, https://doi.org/10.1175/JPO3101.1.

Brannigan, L., D. P. Marshall, A. Naveira-Garabato, and A. J. G. Nurserc, 2015: The seasonal cycle of submesoscale flows. *Ocean Modell.*, **92**, 69–84, https://doi.org/10.1016/j.ocemod.2015.05.002.

Buckingham, C. E., 2016: Seasonality of submesoscale flows in the ocean surface boundary layer. *Geophys. Res. Lett.*, **43**, 2118–2126, https://doi.org/10.1002/2016GL068009.

Bühler, O., J. Callies, and R. Ferrari, 2014: Wave-vortex decomposition of one-dimensional ship-track data. *J. Fluid Mech.*, **756**, 1007–1026, https://doi.org/10.1017/jfm.2014.488.

Callies, J., R. Ferrari, J. Klymak, and J. Gula, 2015: Seasonality in submesoscale turbulence. *Nat. Commun.*, **6**, 6862, https://doi.org/10.1038/ncomms7862.

Capet, X., J. C. McWilliams, M. J. Molemaker, and A. F. Shchepetkin, 2008: Mesoscale to submesoscale transition in the California current system: Flow structure, eddy flux, and observational tests. *J. Phys. Oceanogr.*, **38**, 29–43, https://doi.org/10.1175/2007JPO3671.1.

Chelton, D. B., M. G. Schlax, R. M. Samelson, and R. A. de Szoeke, 2007: Global observations of large oceanic eddies. *Geophys. Res. Lett.*, **34**, L15606, https://doi.org/10.1029/2007GL030812.

——, ——, and ——, 2011: Global observations of nonlinear mesoscale eddies. *Prog. Oceanogr.*, **91**, 167–216, https://doi.org/10.1016/j.pocean.2011.01.002.

Clément, L., E. Frajka-Williams, K. L. Sheen, J. A. Brearley, and A. C. N. Garabato, 2016: Generation of internal waves by eddies impinging on the western boundary of the North Atlantic. *J. Phys. Oceanogr.*, **46**, 1067–1079, https://doi.org/10.1175/JPO-D-14-0241.1.

D'Asaro, E. A., L. Lee, L. Rainville, R. Harcourt, and L. Thomas, 2011: Enhanced turbulence and energy dissipation at ocean fronts. *Science*, **332**, 318–322, https://doi.org/10.1126/science.1201515.

de La Lama, M. S., J. H. LaCasce, and H. K. Fuhr, 2016: The vertical structure of ocean eddies. *Dyn. Stat. Climate Syst.*, **1**, dzw001, https://doi.org/10.1093/climsys/dzw001.

Donzis, D. A., and P. K. Yeung, 2010: Resolution effects and scaling in numerical simulations of passive scalar mixing in turbulence. *Physica D*, **239**, 1278–1287, https://doi.org/10.1016/j.physd.2009.09.024.

Dritschel, D. G., and A. Viudez, 2006: The persistence of balance in geophysical flows. *J. Fluid Mech.*, **570**, 365–383, https://doi.org/10.1017/S0022112006002990.

Eckhardt, B., T. M. Schneider, B. Hof, and J. Westerweel, 2007: Turbulence transition in pipe flow. *Annu. Rev. Fluid Mech.*, **39**, 447–468, https://doi.org/10.1146/annurev.fluid.39.050905.110308.

Erickson, Z. K., A. F. Thompson, J. Callies, X. Yu, A. Naveira Garabato, and P. Klein, 2020: The vertical structure of open-ocean submesoscale variability during a full seasonal cycle. *J. Phys. Oceanogr.*, **50**, 145–160, https://doi.org/10.1175/JPO-D-19-0030.1.

Ferrari, R., and C. Wunsch, 2010: The distribution of eddy kinetic and potential energies in the global ocean. *Tellus*, **60A**, 92–108, https://doi.org/10.3402/tellusa.v62i2.15680.

Fu, L., and G. R. Flierl, 1980: Nonlinear energy and enstrophy transfers in a realistically stratified ocean. *Dyn. Atmos. Oceans*, **4**, 219–246, https://doi.org/10.1016/0377-0265(80)90029-9.

Gertz, A., and D. N. Straub, 2009: Near-inertial oscillations and the damping of midlatitude gyres: A modelling study. *J. Phys. Oceanogr.*, **39**, 2338–2350, https://doi.org/10.1175/2009JPO4058.1.

Gula, J., M. J. Molemaker, and J. C. McWilliams, 2015: Topographic vorticity generation, submesoscale instability, and vortex street formation in the Gulf Stream. *Geophys. Res. Lett.*, **42**, 4054–4062, https://doi.org/10.1002/2015GL063731.

——, ——, and ——, 2016: Topographic generation of submesoscale centrifugal instability and energy dissipation. *Nat. Commun.*, **7**, 12811, https://doi.org/10.1038/ncomms12811.

Hof, B., A. Juel, and T. Mullin, 2003: Scaling of the turbulence transition threshold in a pipe. *Phys. Rev. Lett.*, **91**, 244502, https://doi.org/10.1103/PhysRevLett.91.244502.

Isern-Fontanet, E., E. García-Ladona, and J. Font, 2006: Vortices of the Mediterranean sea: An altimetric perspective. *J. Phys. Oceanogr.*, **36**, 87–103, https://doi.org/10.1175/JPO2826.1.

Kaneda, Y., and T. Ishihara, 2006: High-resolution direct numerical simulation of turbulence. *J. Turbul.*, **7**, 1–17, https://doi.org/10.1080/14685240500256099.

LaCasce, J. H., 2017: The prevalence of oceanic surface modes. *Geophys. Res. Lett.*, **44**, 11 097–11 105, https://doi.org/10.1002/2017GL075430.

——, and S. Groeskamp, 2020: Baroclinic modes over rough bathymetry and the surface deformation radius. *J. Phys. Oceanogr.*, **50**, 2835–2847, https://doi.org/10.1175/JPO-D-20-0055.1.

Larichev, V. D., and I. M. Held, 1995: Eddy amplitudes and fluxes in a homogeneous model of fully developed baroclinic instability. *J. Phys. Oceanogr.*, **25**, 2285–2297, https://doi.org/10.1175/1520-0485(1995)025<2285:EAAFIA>2.0.CO;2.

Liang, X., and A. M. Thurnherr, 2012: Eddy-modulated internal waves and mixing on a midocean ridge. *J. Phys. Oceanogr.*, **42**, 1242–1248, https://doi.org/10.1175/JPO-D-11-0126.1.

Lien, R.-C., and T. B. Sanford, 2019: Small-scale potential vorticity in the upper ocean thermocline. *J. Phys. Oceanogr.*, **49**, 1845–1872, https://doi.org/10.1175/JPO-D-18-0052.1.

Lumpkin, R., and S. Elipot, 2010: Surface drifter pair spreading in the North Atlantic. *J. Geophys. Res.*, **115**, C12017, https://doi.org/10.1029/2010JC006338.

McWilliams, J. C., 1984: The emergence of isolated coherent vortices in turbulent flow. *J. Fluid Mech.*, **146**, 21–43, https://doi.org/10.1017/S0022112084001750.

——, 1989: Statistical properties of decaying geostrophic turbulence. *J. Fluid Mech.*, **198**, 199–230, https://doi.org/10.1017/S0022112089000108.

Nadiga, B. T., 2014: Nonlinear evolution of a baroclinic wave and imbalanced dissipation. *J. Fluid Mech.*, **756**, 965–1006, https://doi.org/10.1017/jfm.2014.464.

Naveira Garabato, A. C., X. Yu, J. Callies, R. Barkan, K. L. Polzin, E. E. Frajka-Williams, C. E. Buckingham, and S. M. Griffies, 2022: Kinetic energy transfers between mesoscale and submesoscale motions in the open ocean's upper layers. *J. Phys. Oceanogr.*, **52**, 75–97, https://doi.org/10.1175/JPO-D-21-0099.1.

Okubo, A., 1970: Horizontal dispersion of floatable particles in the vicinity of velocity singularities such as convergences. *Deep-Sea Res.*, **17**, 445–454, https://doi.org/10.1016/0011-7471(70)90059-8.

Poje, A. C., T. M. Ozgokmen, D. J. Bogucki, and A. D. Kirwan, 2017: Evidence of a forward energy cascade and Kolmogorov self-similarity in submesoscale ocean surface drifter observations, *Phys Fluids*, **29**, 020701, https://doi.org/10.1063/1.4974331.

Pope, S. B., 2000: *Turbulent Flows*. Cambridge University Press, 771 pp.

Qiu, B., S. Chen, P. Klein, H. Sasaki, and Y. Sasai, 2014: Seasonal mesoscale and submesoscale eddy variability along the North Pacific subtropical countercurrent. *J. Phys. Oceanogr.*, **44**, 3079–3098, https://doi.org/10.1175/JPO-D-14-0071.1.

——, T. Nakano, S. Chen, and P. Klein, 2017: Submesoscale transition from geostrophic flows to internal waves in the northwestern Pacific upper ocean. *Nat. Commun.*, **8**, 14055, https://doi.org/10.1038/ncomms14055.

——, S. Chen, P. Klein, J. Wang, H. Torres, L. Fu, and D. Menemenlis, 2018: Seasonality in transition scale from balanced to unbalanced motions in the world ocean. *J. Phys. Oceanogr.*, **48**, 591–605, https://doi.org/10.1175/JPO-D-17-0169.1.

Remmel, M., and L. Smith, 2009: New intermediate models for rotating shallow water and an investigation of the preference for anticyclones. *J. Fluid Mech.*, **635**, 321–359, https://doi.org/10.1017/S0022112009007897.

Richman, J. G., B. K. Arbic, J. F. Shriver, E. J. Metzger, and A. J. Wallcraft, 2012: Inferring dynamics from the wavenumber spectra of an eddying global ocean model with embedded tides. *J. Geophys. Res.*, **117**, C12012, https://doi.org/10.1029/2012JC008364.

Rocha, C. B., G. L. Wagner, and W. R. Young, 2018: Stimulated generation-extraction of energy from balanced flow by near-inertial waves. *J. Fluid Mech.*, **847**, 417–451, https://doi.org/10.1017/jfm.2018.308.

Rudnick, D. L., 2001: On the skewness of vorticity in the upper ocean. *Geophys. Res. Lett.*, **28**, 2045–2048, https://doi.org/10.1029/2000GL012265.

Salmon, R., 1998: *Lectures on Geophysical Fluid Dynamics*. Oxford University Press, 378 pp.

Savage, A., and Coauthors, 2017: Spectral decomposition of internal gravity wave sea surface height in global models. *J. Geophys. Res. Oceans*, **122**, 7803–7821, https://doi.org/10.1002/2017JC013009.

Scott, R. B., and F. M. Wang, 2005: Direct evidence of an oceanic inverse kinetic energy cascade from satellite altimetry. *J. Phys. Oceanogr.*, **35**, 1650–1666, https://doi.org/10.1175/JPO2771.1.

Shcherbina, A. Y., E. A. D'Asaro, C. Lee, J. M. Klymak, M. J. Molemaker, and J. C. McWilliams, 2013: Statistics of vertical vorticity, divergence, and strain in a developed submesoscale turbulence field. *Geophys. Res. Lett.*, **40**, 4706–4711, https://doi.org/10.1002/grl.50919.

Smith, K. S., and G. K. Vallis, 2001: The scales and equilibration of midocean eddies: Freely evolving flow. *J. Phys. Oceanogr.*, **31**, 554–571, https://doi.org/10.1175/1520-0485(2001)031<0554:TSAEOM>2.0.CO;2.

Taylor, S., and D. Straub, 2016: Forced near-inertial motion and dissipation of low-frequency kinetic energy in a wind-driven channel flow. *J. Phys. Oceanogr.*, **46**, 79–93, https://doi.org/10.1175/JPO-D-15-0060.1.

——, and ——, 2020: Effects of adding forced near-inertial motion to a wind-driven channel flow. *J. Phys. Oceanogr.*, **50**, 2983–2996, https://doi.org/10.1175/JPO-D-19-0299.1.

Tchilibou, M., L. Gourdeau, R. Morrow, G. Serazin, B. Djath, and F. Lyard, 2018: Spectral signatures of the tropical Pacific dynamics from model and altimetry: A focus on the meso/submesoscale range. *Ocean Sci.*, **14**, 1283–1301, https://doi.org/10.5194/os-14-1283-2018.

Thomas, J., and R. Yamada, 2019: Geophysical turbulence dominated by inertia-gravity waves. *J. Fluid Mech.*, **875**, 71–100, https://doi.org/10.1017/jfm.2019.465.

——, and S. Arun, 2020: Near-inertial waves and geostrophic turbulence. *Phys. Rev. Fluids*, **5**, 014801, https://doi.org/10.1103/PhysRevFluids.5.014801.

——, and D. Daniel, 2020: Turbulent exchanges between near-inertial waves and balanced flows. *J. Fluid Mech.*, **902**, A7, https://doi.org/10.1017/jfm.2020.510.

——, and ——, 2021: Forward flux and enhanced dissipation of geostrophic balanced energy. *J. Fluid Mech.*, **911**, A60, https://doi.org/10.1017/jfm.2020.1026.

——, K. Smith, and O. Bühler, 2017: Near-inertial wave dispersion by geostrophic flows. *J. Fluid Mech.*, **817**, 406–438, https://doi.org/10.1017/jfm.2017.124.

Thompson, A. F., A. Lazar, C. E. Buckingham, A. C. Naveira Garabato, G. M. Damerell, and K. J. Heywood, 2016: Open-ocean submesoscale motions: A full seasonal cycle of mixed layer instabilities from gliders. *J. Phys. Oceanogr.*, **46**, 1285–1307, https://doi.org/10.1175/JPO-D-15-0170.1.

Torres, H. S., P. Klein, D. Menemenlis, B. Qiu, Z. Su, J. Wang, S. Chen, and L.-L. Fu, 2018: Partitioning ocean motions into balanced motions and internal gravity waves: A modeling study in anticipation of future space missions. *J. Geophys. Res. Oceans*, **123**, 8084–8105, https://doi.org/10.1029/2018JC014438.

Wagner, G. L., and W. R. Young, 2016: A three-component model for the coupled evolution of near-inertial waves, quasi-geostrophic flow and the near-inertial second harmonic. *J. Fluid Mech.*, **802**, 806–837, https://doi.org/10.1017/jfm.2016.487.

Weiss, J., 1991: The dynamics of enstrophy transfer in two-dimensional hydrodynamics. *Physica D*, **48**, 273–294, https://doi.org/10.1016/0167-2789(91)90088-Q.

Wunsch, C., 1997: The vertical partition of oceanic horizontal kinetic energy and the spectrum of global variability. *J. Phys. Oceanogr.*, **27**, 1770–1794, https://doi.org/10.1175/1520-0485(1997)027<1770:TVPOOH>2.0.CO;2.

——, and D. Stammer, 1998: Satellite altimetry, the marine geoid and the oceanic general circulation. *Annu. Rev. Earth Planet. Sci.*, **26**, 219–253, https://doi.org/10.1146/annurev.earth.26.1.219.

Xie, J.-H., 2020: Downscale transfer of quasigeostrophic energy catalyzed by near-inertial waves. *J. Fluid Mech.*, **904**, A40, https://doi.org/10.1017/jfm.2020.709.

——, and J. Vanneste, 2015: A generalised-lagrangian-mean model of the interactions between near-inertial waves and mean flow. *J. Fluid Mech.*, **774**, 143–169, https://doi.org/10.1017/jfm.2015.251.

Xu, Y., and L.-L. Fu, 2011: Global variability of the wavenumber spectrum of oceanic mesoscale turbulence. *J. Phys. Oceanogr.*, **41**, 802–809, https://doi.org/10.1175/2010JPO4558.1.

Yang, Q., W. Zhao, X. Liang, J. Dong, and J. Tian, 2017: Elevated mixing in the periphery of mesoscale eddies in the South China Sea. *J. Phys. Oceanogr.*, **47**, 895–907, https://doi.org/10.1175/JPO-D-16-0256.1.

Yu, X., A. C. Naveira Garabato, A. P. Martin, C. E. Buckingham, L. Brannigan, and Z. Su, 2019: An annual cycle of submesoscale vertical flow and restratification in the upper ocean. *J. Phys. Oceanogr.*, **49**, 1439–1461, https://doi.org/10.1175/JPO-D-18-0253.1.

Zhao, M., M.-L. Timmermans, R. Krishfield, and G. Manucharyan, 2018: Partitioning of kinetic energy in the Arctic Ocean's Beaufort Gyre. *J. Geophys. Res. Oceans*, **123**, 4806–4819, https://doi.org/10.1029/2018JC014037.